Evolution of microstructure, macrotexture and mechanical properties of commercially pure Ti during ECAP-conform processing and drawing

D.V. Gunderov , A.V. Polyakov , I.P. Semenova , G.I. Raab , A.A. Churakova , E.I. Gimaltdinova , I. Sabirov , J. Segurado , V.D. Sitdikov , I.V. Alexandrov , N.A. Enikeev , R.Z. Valiev

A B S T R A C T

Long-length ultrafine-grained (UFG) Ti rods are produced by equal-channel angular pressing via the conform scheme (ECAP-C) at 200 °C, which is followed by drawing at 200 °C. The evolution of microstructure, macrotexture, and mechanical properties (yield strength, ultimate tensile strength, failure stress, uniform elongation, elongation to failure) of pure Ti during this thermo-mechanical processing is studied. Special attention is also paid to the effect of microstructure on the mechanical behavior of the material after macrolocalization of plastic flow. The number of ECAP-C passes varies in the range of 1–10. The microstructure is more refined with increasing number of ECAP-C passes. Formation of homogeneous microstructure with a grain/subgrain size of 200 nm and its saturation after 6 ECAP-C passes are observed. Strength properties increase with increasing number of ECAP passes and saturate after 6 ECAP-C passes to a yield strength of 973 MPa, an ultimate tensile strength of 1035 MPa, and a true failure stress of 1400 MPa (from 625, 750, and 1150 MPa in the as-received condition). The true strain at failure decreases after ECAP-C processing. The reduction of area and true strain to failure values do not decrease after ECAP-C processing. The sample after 6 ECAP-C passes is subjected to drawing at 200°C resulting in reduction of a grain/subgrain size to 150 nm, formation of $(10\bar{1}0)$ fiber texture with respect to the rod axis, and further increase of the yield strength up to 1190 MPa, the ultimate tensile strength up to 1230 MPa and the true failure stress up to 1600 MPa. It is demonstrated that UFG CP Ti has low resistance to macrolocalization of plastic deformation and high resistance to crack formation after necking.

1. Introduction

Due to high corrosion resistance and biocompatibility commercially pure (CP) titanium has been widely used for production of medical implants [1]. However, its mechanical strength is lower compared to that of other alloys used for producing biomedical devices [1]. Alloying can significantly enhance mechanical performance of CP Ti, but some alloying elements such as vanadium increase the toxicity of CP Ti. Nowadays, development of severe plastic deformation (SPD) [2] techniques has made it possible to form ultrafine-grained (UFG) microstructure in CP Ti, which resulted in enhancement of its mechanical strength. These SPD techniques include high pressure torsion (HPT) [3,4], equal-channel angular pressing (ECAP) [5,6], ECAP in combination with extrusion and/or rolling [7,8], hydrostatic extrusion [9,10], cryo-rolling followed by annealing [11], etc.

There is a body of research into the deformation behavior of ultra-fine-grained (UFG) CP Ti processed via equal channel angular pressing (ECAP) [12,13], high-pressure torsion [14,15] and hydrostatic extrusion [16]. It has been demonstrated that combination of various thermomechanical processing methods can be successfully applied to improve mechanical properties of pure Ti—up to 1000 MPa [17–19].

One of new modifications of ECAP processing is an ECAP-Conform (ECAP-C) technique that allows fabricating UFG microstructure in long-length rods (up to few meters long) suitable for commercial applications [20–22]. However, in order to realize this specific procedure, especially in combination with various post-SPD treatment one needs to gain a fundamental understanding of the deformation mechanisms and to reveal correlation between SPD-induced nanostructures and properties of materials. The properties of SPD materials strongly depend not only on a refined grain size but

also on other microstructural features such as grain boundaries state, defect densities, texture, misorientation spectra etc. In its turn, the variety of nanostructural features is caused by different processing parameters such as temperature, strain and strain rate, processing route, die-set design, friction, etc. Thus, the task of producing nanostructured samples with microstructures providing the best set of output properties is complicated and multifactorial.

This task could hardly be solved without employing models considering the processes occurring on different levels during SPD processing. Influence of SPD processing parameters and subsequent conventional treatment (strain, strain rate, temperature, friction conditions, die design, pressure, routes, modes) on the peculiarities of material flow during deformation could be studied on the macrolevel by finite element models [23]. Acting slip systems, grain shaping and crystallographic texture formation may be identified on the mesolevel [24]. In addition, multiscale plasticity approaches coupling the macroscopic simulation of the SPD process with local micromechanical crystal plasticity models can be used for assessing microstructure heterogeneity of SPD processed samples [24–26], and polycrystalline homogenization models as VPSC can be implicitly embedded into the FEM simulation routine [27]. Fragmentation models are developed on the microlevel to describe the grain refinement process and to provide data on such vital parameters of resulting nanostructures as grain size and grain boundary misorientation spectra [28–30]. Kinetic dislocation models are used for simulating microstructure evolution and mechanical properties of SPD-processed materials [31,32], and the models also could be coupled with FEM simulation [33].

Bio-medical industry producing nanostructured Ti implants could benefit from such multi-level models. However, multiscale simulation procedures require a large amount of experimental data to be used as input parameters for computational models as well as for validation of these models. Thus, the main objective of this work is to study the evolution of microstructure, macrotexture, and mechanical properties of CP Ti (Grade 4) processed by ECAP-C and following post-treatment (drawing) in detail. Special attention is paid to the effect of microstructure on the mechanical behavior of the material after macrolocalization of plastic flow, to the true failure stress and strain to failure. The "processing–microstructure–mechanical properties" relationship in the studied material is discussed.

2. Material and experimental procedures

CP Ti (Grade 4) in the shape of hot-rolled rods with a diameter of 12 mm (manufactured by Dynamet Company) was used in investigations. Table 1 presents the impurity content in the material. The average grain size of the as-received material was 25 μm.

Table 1
Impurity content in CP Ti Grade 4 (according to the certificate wt.%).

Ti	C	Fe	N	H	O
Base	0.04	0.14	0.006	0.0015	0.36

Billets 500 mm in length and 11×11 mm^2 in cross section were subjected to ECAP-C processing at 200 °C with a different number of passes ($n = 1, 2, 4, 6, 8$, and 10). The principle of ECAP-C processing is presented schematically in Fig. 1a. The channels intersection angle was 120 °C, which facilitated accumulation of strain ~0.7 per each ECAP-C pass.

A piece with a length of 50 mm was cut from each processed rod to study its microstructure and mechanical tensile properties. The billet with a cross section of 11×11 mm^2 after 6 ECAP-C passes was subjected to drawing at 200 °C resulting in production of a rod with a diameter of 6 mm.

The microstructure was analyzed by the optical and transmission electron microscopies (TEM). The processed rods were examined in 2 sections: those are cross section plane YZ and longitudinal section plane XZ, as shown in Fig. 1a. For optical metallography, the sample surface was polished mechanically and etched in chemical solution consisting of hydrofluoric acid −4%, perchloric acid −20%, and distilled water −76%. Samples for TEM studies were cut out by the electrospark method according to the scheme shown in Fig. 1b. After mechanical thinning down to 100 μm, they were subjected to electrolytic polishing using a "Tenupol-5" set. Electropolishing was conducted using chemical solution consisting of perchloric acid −5%, butanol −35% and methanol −60% at the temperature range of −20…−35 °C. The microstructure was investigated in a JEOL JEM 2100 TEM operating at an accelerating voltage of 200 kV.

X-ray studies were carried out using a Rigaku Ultima IV diffractometer. The geometric center of the cross section was investigated (plane 2–3) (Fig. 1c). The studies were conducted using Cu K_α irradiation (45 kV, 30 mA) and a plane monochromator on the reflected beam. The wave length $\lambda K_{\alpha 1} = 1.540598$ Å was used for calculations. A general view of X-ray diffraction patterns was taken within the range of angles 2θ from 30° to 140° with a scanning step of 0.05°, and exposure time was 3 s at every point. Data registration of the chosen X-ray peaks within the range from 30° to 140° was performed with a scanning step 0.01° and an exposure time of 10 s for higher-precision studies. PDXL software by Rigaku was employed for the quantitative evaluation of coherent-scattering domain sizes and mean-square microdistortions. Dislocation density was calculated according to the method developed in Ref. [34]. Macrotexture measurements were performed using a DRON-3M diffractometer equipped with an automatic texture set. The diameter of the irradiated area was ~0.6 mm. Incomplete pole figures were measured using filtered X-ray beaming of Cu $K_{\alpha 1}$ (0.1540598 nm). The experiment was conducted over the range of the radial angle γ from 0° to 75° and azimuthal angle δ from 0° to 360°. Consequently, a set of intensities of reflected X-rays $P_{hkl}(y)$ was obtained. The experiment results were presented as complete pole figures generated with the LaboTEX software [35].

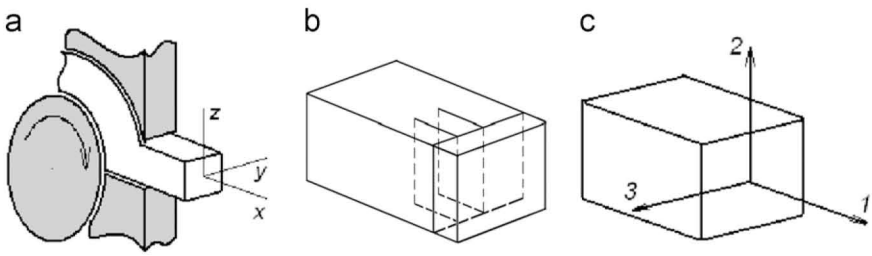

Fig. 1. Orientation of XZ and YZ planes in a sample during ECAP-C processing (a) and scheme of samples cutting for foils for TEM studies (b); scheme of the area examined by X-ray (c).

Mechanical tensile tests were conducted at room temperature with the initial strain rate of $10^{-3}\,s^{-1}$ using an INSTRON-type testing machine. Cylindrical samples with a gauge length of 15 mm and a diameter of 3 mm were tested. At least 2 samples were tested for each material condition, and the results were found to be reproducible. Mechanical properties (yield strength, ultimate tensile strength, maximum true stress in homogeneous plastic flow, true stress at failure, uniform elongation, elongation to failure, maximum strain at the neck, and reduction of the area in the neck) were determined for each material condition.

3. Results and discussion

3.1. Evolution of microstructure in CP Ti during ECAP-C processing and drawing

TEM analysis of the microstructure showed that substructure forms in CP Ti after the first and second ECAP-C passes (Fig. 2a). This microstructure is characterized by a high fraction of low-angle boundaries, enhanced dislocation density (6×10^{14} to $8\times10^{14}\,m^{-2}$), and deformation twins having a size comparable to the grain size. Deformation twinning is supposed to play a key role in formation of elongated grains and accommodation of a large amount of shear strain induced by ECAP-C. It should be noted that such microstructures are typical of Ti subjected to low-strain deformation via conventional ECAP [6,13,38].

Misorientations of subgrain boundaries grow with equivalent strain increasing to ~2.8 (Fig. 2b). Table 2 lists average grain sizes in the cross and longitudinal directions of ECAP-C processed rods (number of investigated grains ~150). The size of grains/subgrains measured using bright field TEM images is approximately 300 nm (Table 2). The microstructure is very inhomogeneous with a much higher dislocation density ($9\times10^{14}\,m^{-2}$) as compared to that reported for CP Ti after conventional ECAP [13] due to the lower processing temperature of 200 °C vs. 450 °C applied in conventional ECAP [38].

Table 2
Average grain size D of Ti Grade 4 after ECAP-C in the cross and longitudinal sections measured from bright-field TEM images (standard deviation for grain size is nearly 20 nm in all measurements).

Number of ECAP-C cycles	***n*=4**		***n*=6**		***n*=8**	
Section	Cross	Longitudinal	Cross	Longitudinal	Cross	Longitudinal
Grain size (μm)	230	230	174	220	195	230

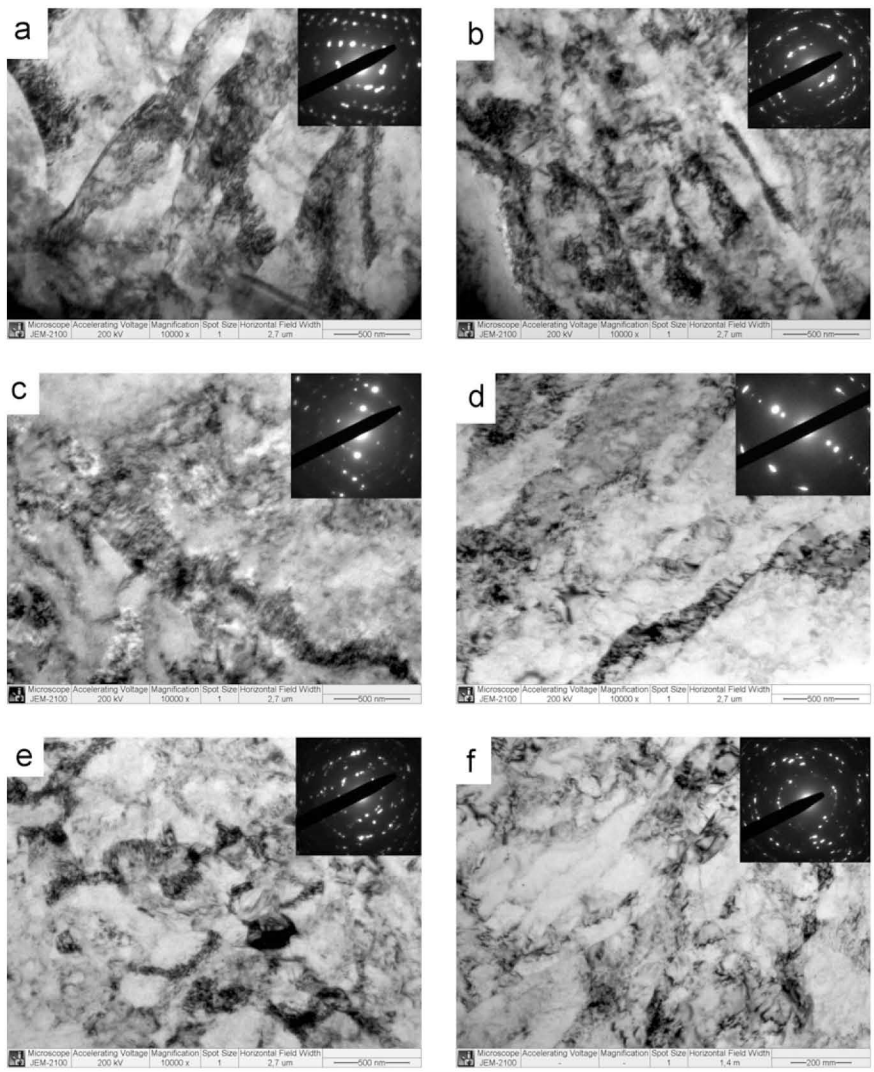

Fig. 2. Bright-field TEM images of CP Ti after 1, 2, and 4 ECAP-C passes in cross and longitudinal sections. Cross section: (a) 1 pass, (c) 2 passes and (e) 4 passes; Longitudinal section: (b) 1 pass, (d) 2 passes and (f) 4 passes.

The grain/subgrain size decreases down to ~200 nm with further increase of the number of ECAP-C passes to 6–8 (Fig. 3), whereas the fraction of high-angle grain boundaries and the dislocation density increase (Table 3). This can be also proved by dramatic increase in the number of spots in the electron-diffraction patterns (Fig. 3). It is seen from Fig. 3c and d that the grains have an equi-axed shape, and the grain boundaries are well defined in the bright-field TEM images. Fig. 4 displays the histograms of grain size distribution. The aspect ratio of grains in the longitudinal and cross sections was about 0.6. The histograms of grain size distribution in CP Ti (Grade 4) after 6 ECAP-C passes have the "Gaussian" character with some deviation due to the presence of some coarse grains having the size up to 1.5 μm. Similar microstructure was also observed in the material after 10 ECAP-C passes (ε=7.0).

After 6 ECAP-C passes and subsequent drawing with an equivalent strain of 0.6, formation of very homogeneous ultra-fine grained microstructure with the average grain/subgrain size of ~150 nm is observed (Fig. 5).

The comparative analysis of the microstructural parameters derived from the X-ray studies showed that the sizes of coherently scattering domains (CSD), the levels of elastic microdistortions of a crystal lattice $\langle \varepsilon^2 \rangle$, and the dislocation density ρ in CP Ti after ECAP-C processing are significantly different compared to those in the as-received condition (Table 3). The CSD size in the as-received condition is 70 nm. The CSD-value decreases, with the number of ECAP-C passes increasing, and saturates at 28 ± 3 nm after 2 ECAP-C passes (Table 2), which is similar to the results reported in Ref. [36] for CP Ti (Grade 2) subjected to 8 ECAP passes. On the contrary, elastic microdistortions and dislocation density significantly increase with the number of ECAP-C passes increasing.

3.2. Evolution of macrotexture in CP Ti during ECAP-C processing and drawing

Fig. 6 illustrates experimental PFs for CP Ti before and after ECAP-C processing. The position of texture maxima on the

Table 3
Microstructural parameters derived from the X-ray analysis.

Condition	CSD (nm)	$\langle \varepsilon^2 \rangle \times 10^{-4}$	$\rho \times 10^{15}$ (m^{-2})
Initial	70 ± 10	7 ± 1	~0.13
After 1 ECAP-C pass	31 ± 3	15 ± 2	~0.58
After 2 ECAP-C passes	28 ± 3	19 ± 2	~0.79
After 4 ECAP-C passes	26 ± 3	21 ± 2	~0.90
After 8 ECAP-C passes	25 ± 2	25 ± 2	~1.17

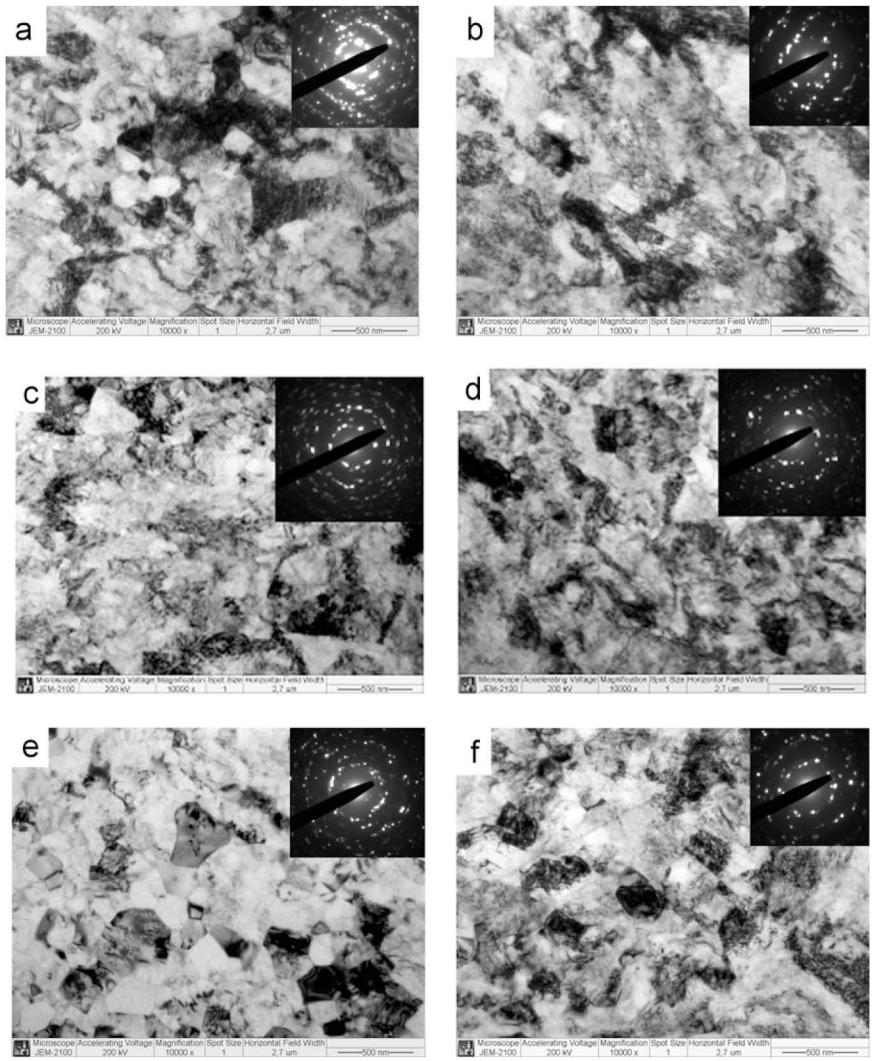

Fig. 3. Bright-field TEM images of CP Ti Grade 4 after 8 and 10 ECAP-C passes in cross and longitudinal sections. Cross section: (a) 6 passes, (c) 8 passes and (e) 10 passes; Longitudinal section: (b) 6 passes, (d) 8 passes and (f) 10 passes.

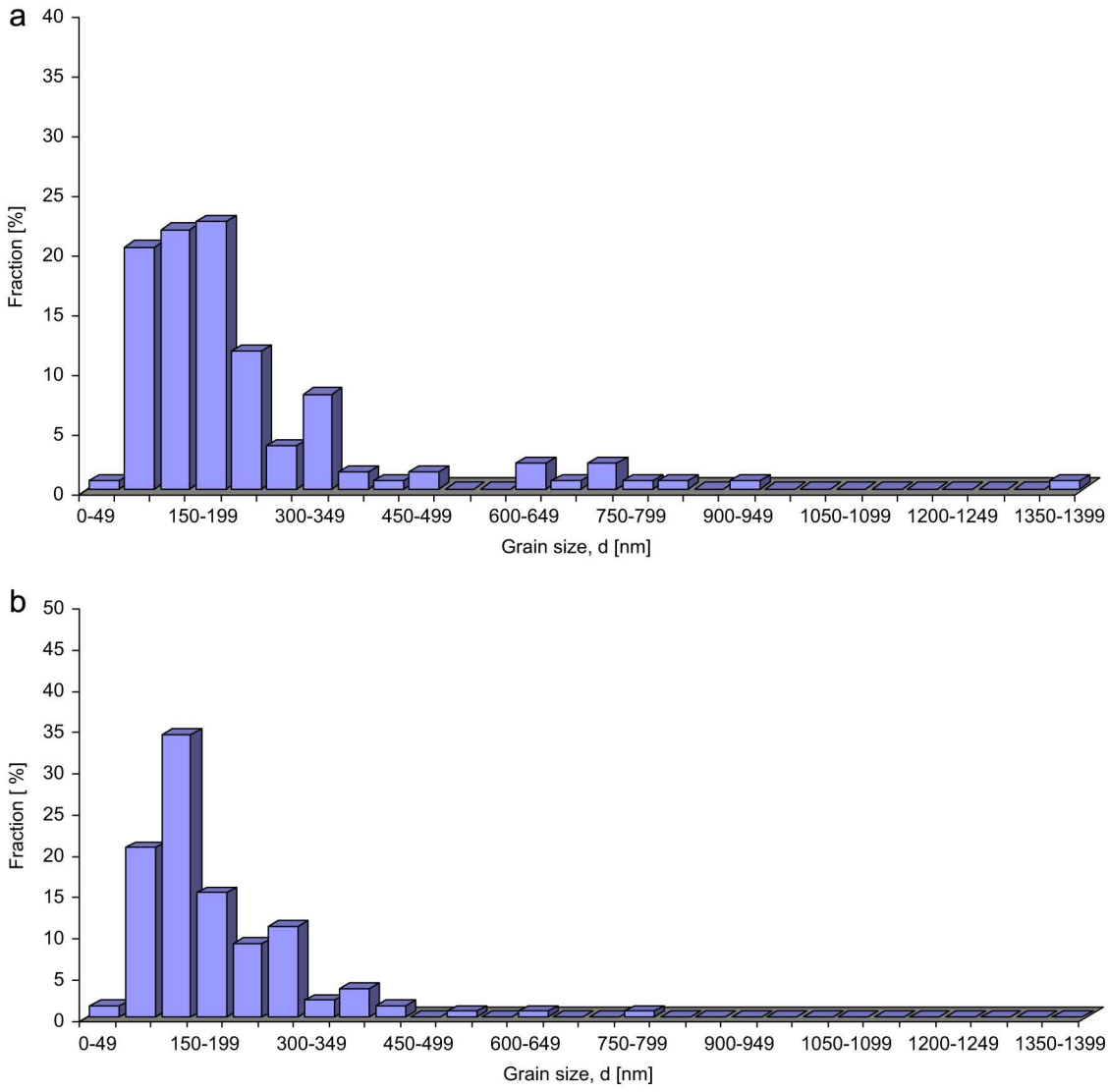

Fig. 4. Histograms of grain size distribution in CP Ti after ECAP-C for 6 passes in the longitudinal (a) and cross (b) sections.

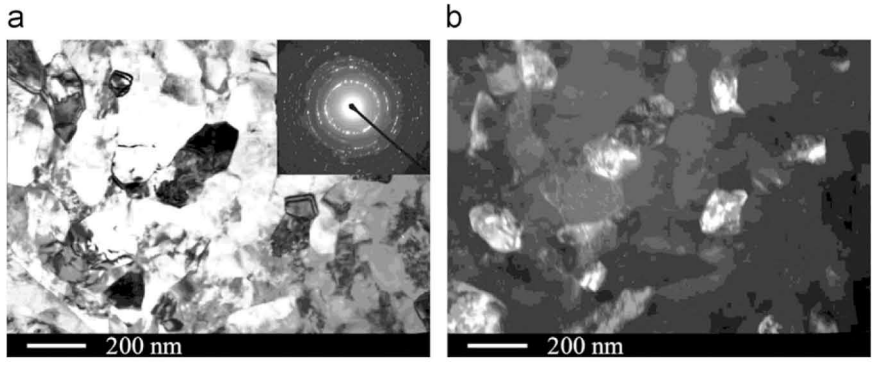

Fig. 5. Bright-field (a) and dark-field (b) TEM images of CP Ti Grade 4 after 6 ECAP-C passes and drawing.

experimental PFs for the as-received condition (Fig. 6a) is typical of CP Ti deformed by hot rolling. Basic $\{0001\}\langle 01\bar{1}0\rangle$ and prismatic $\{10\bar{1}0\}\langle 01\bar{1}0\rangle$ components of the texture prevail, which are active in coarse-grained Ti [37]. It is observed that main texture maxima are located in their center.

The first ECAP-C pass predetermines the character of further evolution of preferred crystallographic orientations of grains. The nature of texture maxima arrangement on PF (0002) points at the fact that basal planes are arranged mainly in parallel to the shear plane (the plane of channels intersection), and, therefore, they are favorably oriented for sliding of $\langle a\rangle$ dislocations along this plane, as well as along prismatic and pyramidal planes of the first and second orders in the $\langle a\rangle$ and $\langle a+c\rangle$ directions (Fig. 6). This texture exhibits 2 main texture maxima $\{01\bar{1}2\}\langle 12\bar{3}1\rangle$ and $\{01\bar{1}0\}\ \langle 10\bar{1}0\rangle$.

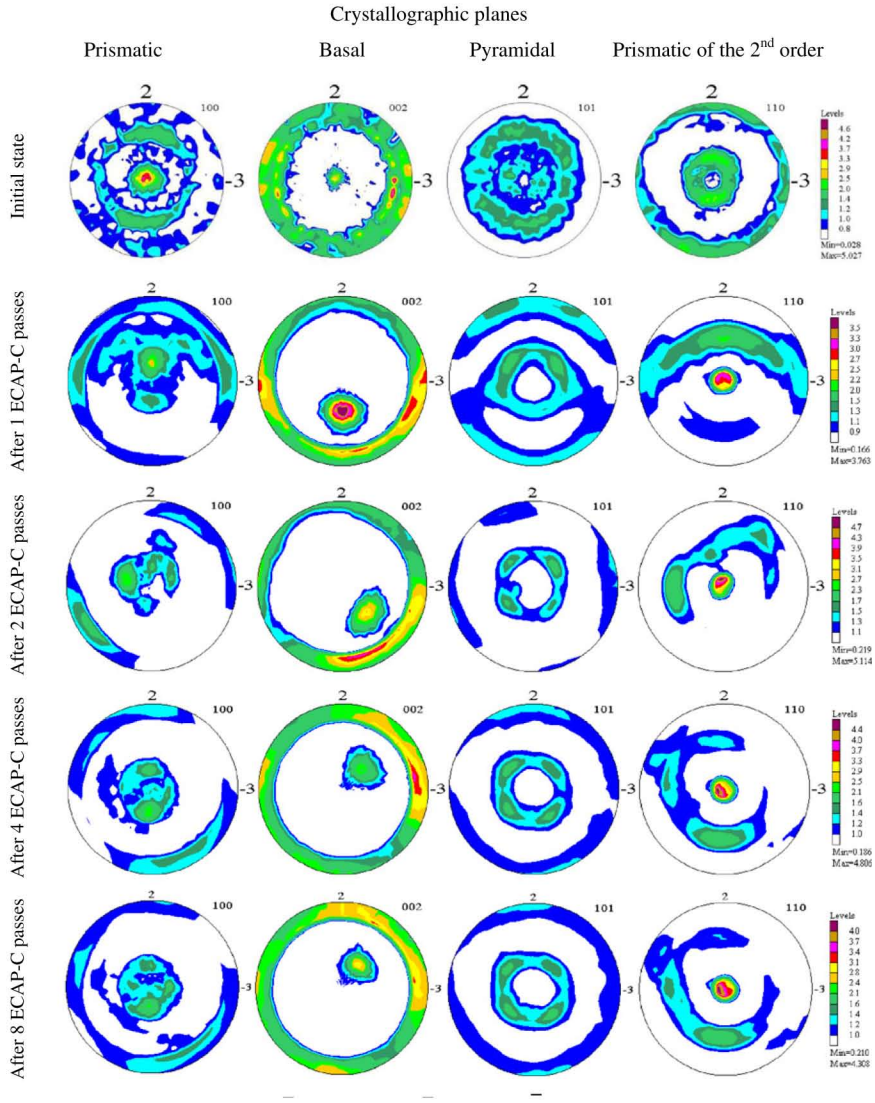

Fig. 6. Experimental PFs for $(10\bar{1}0)$, (0002), $(10\bar{1}1)$, and $(11\bar{2}0)$ planes in CP Ti Grade 4 before and after ECAP-C processing.

During the second pass the texture maxima arrangement changes, which testifies to changes in preferred crystallographic orientations (Fig. 6). The basal plane that was parallel to the shear plane after the 1st pass rotates counterclockwise by 45° around axis 1 (Fig. 6). A new texture maximum $\{000\bar{1}\}\langle 32\bar{5}0\rangle$ appears, which is close to the PF center. Besides, the pole density of texture maxima with Miller indices $\{01\bar{1}0\}\ \langle 10\bar{1}0\rangle$ and $\{\bar{1}010\}\ \langle 01\bar{1}0\rangle$ enhances on the (0002) PF periphery (Fig. 6).

After the 4th pass the PFs change again (Fig. 6). Generally they look similar to those after the 2nd pass, if they are rotated around axis 1 by 90°. After the 4th pass a new texture maximum $\{01\bar{1}2\}\langle\bar{3}25\bar{5}\rangle$ close to the PF center appears on (0001) PF, i.e. the maximum $(000\bar{1})[32\bar{5}0]$ transits to $\{01\bar{1}2\}\langle\bar{3}25\bar{5}\rangle$. Besides, the intensity of the texture maximum $\{01\bar{1}0\}\langle 10\bar{1}0\rangle$ increases.

After the 8th pass the sample makes a complete rotation about axis 1, and the PFs have the view similar to that after the 4th pass (Fig. 6). However, the pole density of orientation $\{01\bar{1}2\}\langle\bar{3}25\bar{5}\rangle$ increases. At the same time the intensities of the texture maxima $\{01\bar{1}0\}\langle 10\bar{1}0\rangle$ and $\{\bar{1}010\}\ \langle 01\bar{1}0\rangle$ increase (Fig. 6). It should be noted that in the case of conventional ECAP, dislocation slip along basal planes prevails [37], whereas in the case of ECAP-C dislocation slip in basal planes is hindered. It may be associated with lower processing temperature (ECAP at 450°C, ECAP-C at 200 °C).

Fig. 7 demonstrates experimental PFs for CP Ti after 6 ECAP-C passes and drawing. The texture can be described as $(10\bar{1}0)$ fiber one with respect to the rod axis. Such texture is typical of CP Ti after swaging and/or drawing [39]. The sharpness of the texture maxima increases dramatically. The activity of slip systems in hcp pure Ti depends on the value of critical resolved shear stress for these slip systems. For CP Ti, the critical resolved shear stress values are 90 MPa for the prismatic slip system, 105 MPa for the pyramidal $\langle a\rangle$ slip systems, 115 MPa for the basal slip system, and 280 MPa for the pyramidal $\langle a+c\rangle$ slip systems [40]. During drawing along axis 1, the basal and prismatic slip systems of the second type are most favorably oriented for slip of dislocations during straining (Fig. 7).

3.3. The effect of ECAP-C and drawing on mechanical properties of CP Ti

The results of mechanical tensile tests are listed in Table 4, and typical engineering stress–strain curves are presented in Fig. 8. A big increment in the ultimate tensile strength (from 750 to 875 MPa) observed after the 1st ECAP-C pass (Table 4) is mainly

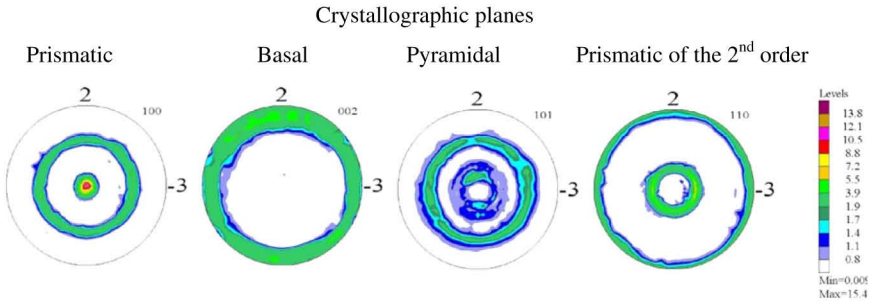

Fig. 7. Experimental PFs $(10\bar{1}0)$, (0002), $(10\bar{1}1)$ and $(11\bar{2}0)$ for CP Ti Grade 4 after 6 ECAP-C passes and subsequent drawing.

Table 4
Mechanical properties of CP Ti in the as-received condition, after ECAP-C processing, and after drawing (YS—yield strength, UTS—ultimate tensile strength, UTS_{true}—maximum true stress in homogeneous flow, δ—elongation to failure, δ_{unif}—uniform elongation, Ψ—reduction of area, e—true strain at failure, σ_{ifail}—true stress at failure).

Condition	*YS* (MPa)	*UTS* (MPa)	UTS_{true} (MPa)	δ (%)	δ_{unif} (%)	Ψ (%)	e	σ_{ifail} (MPa)
as-received	625	760	836	29.3	9.75	50	0.7	920
ECAP-C $n=1$	853	875	895	15.7	2.1	54	0.77	1220
ECAP-C $n=2$	869	884	900	13.7	1.8	55	0.8	1330
ECAP-C $n=4$	921	962	975	16.2	1.6	59	0.87	1420
ECAP-C $n=6$	973	1020	1035	13.7	1.6	54	0.82	1480
ECAP-C $n=8$	966	1030	1045	13.4	1.6	58	0.87	1480
ECAP-C $n=10$	950	1020	1035	14.3	1.6	54	0.8	1440
ECAP-C $n=6$ +drawing	1190	1230	1250	11	1.6	50	0.7	1600

due to strong fragmentation of the microstructure and increased dislocation density in the processed material. The mechanical strength of CP Ti enhances with increasing the number of ECAP-C passes, and saturates after 6 ECAP-C passes (equivalent strain of ~4), and the ultimate tensile strength value is about 1020 MPa (Table 3). This can be related to formation of UFG microstructure with an average grain/subgrain size of ~250 nm and its saturation along with the saturation of the macrotexture after 6 ECAP-C passes (see Sections 3.1 and 3.2). Both uniform elongation and elongation to failure decrease, when the number of ECAP-C passes increases, due to formation of UFG microstructure and very high dislocation density in the as-ECAP-PC microstructure. The UFG microstructure and increased dislocation density lead to significant reduction of work hardening rate during tensile deformation resulting in necking at the earlier stages of plastic deformation. Uniform elongation and elongation to failure tend to saturate after 6 ECAP-C passes due to saturation of both microstructure and texture.

Fig. 9 presents true stress–strain curves for as-received and ECAP-C processed materials. It is clearly seen that the true failure stress in all as-ECAP-PC samples is significantly higher compared to the maximum true stress in homogeneous flow, whereas in the as-received material this difference is low. The uniform elongation in the samples after ECAP-PC processing decreases by a factor of ~6 (from 9.75% to 1.6%), whereas the elongation to failure decreases by a factor of ~2 (from 29.3% to ~14%). Therefore, it can be concluded that the UFG Ti has low resistance to macrolocalization of plastic deformation. The reduction of area ψ and the true failure strain in the neck e are higher for the as-ECAP-C materials compared to those for the as-received Ti. Both ψ- and e-values do not change much with increasing the number of ECAP-C passes (Table 4). After necking the true strain at failure in the neck is determined by the material resistance to crack(s) formation and material resistance to growth of formed crack(s). Since the total crack growth resistance in the UFG CP Ti is lower compared to that in the coarse-grained CP Ti [41], it can be concluded that the increased true strain at failure in the neck in the ECAP-C processed Ti is due to its increased resistance to crack(s) formation.

Drawing of CP Ti after 6 ECAP-C passes leads to significant increase of its mechanical strength: the yield strength increases up to 1190 MPa and the ultimate tensile strength up to 1230 MPa (Table 3). This can be related to (1) decrease of the grain size down to 150 nm (see Sections 3.1) and (2) formation of $(10\bar{1}0)$ fiber texture with basal planes parallel to the rod axis (see Section 3.2). In these tensile specimens 2 of the prismatic slip planes having the lowest critical resolved shear stress are suppressed, since they are perpendicular to the tensile axis. The rest 4 slip planes are inclined at 60° to the tensile axis and can be active. The limited number of available prismatic slip systems provides extra strength to the material. It should be noted that drawing does not affect the uniform elongation, but slightly reduces the elongation to failure (Table 4).

4. Conclusions

CP Ti is subjected to ECAP-C processing at 200 °C, which is followed by drawing at 200 °C. The evolution of microstructure, texture, and mechanical properties during processing is analyzed. The results can be generalized as follows:

1. The microstructure is more refined, and the fraction of high-angle grain boundaries grows with increasing number of ECAP-C passes. Six ECAP-C passes lead to formation of homogeneous ultra-fine grained microstructure with equi-axed grains/subgrains having the size of 200 nm. Both the microstructure and crystallographic texture saturate after this processing.
2. The CP Ti strength enhances with increasing the number of ECAP-C passes and saturates after 6 ECAP-C passes. The ductility of CP Ti shows the opposite tendency.
3. The homogeneous ultrafine-grained microstructure with equi-axed grains/subgrains having the average grain size of 150 nm is formed after drawing of the as-ECAP-C CP Ti. Drawing also leads to formation of $(10\bar{1}0)$ fiber texture with respect to the rod axis with basal planes parallel to the rod axis. This microstructure and texture lead to further enhancement of strength properties of CP Ti without significant sacrifice of its ductility.
4. ECAP-C processed CP Ti shows increased resistance to crack formation during necking.

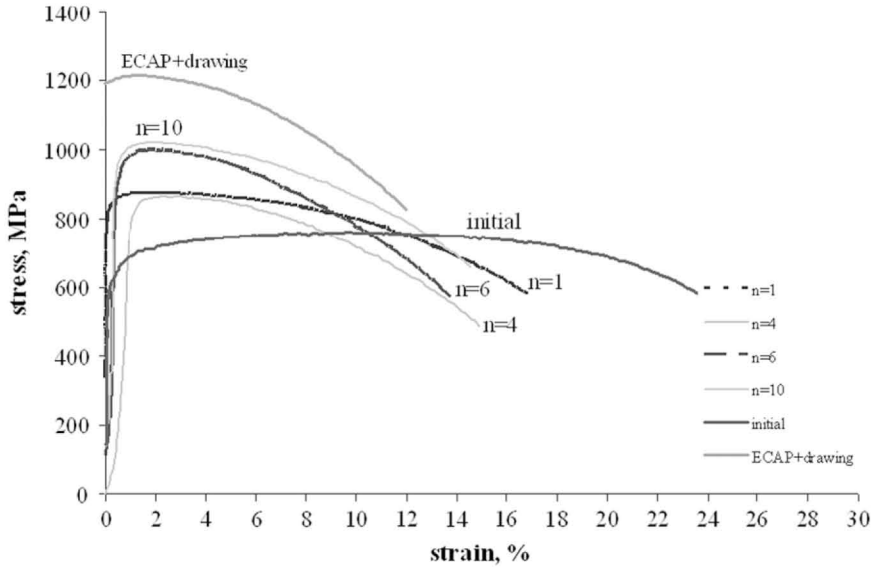

Fig. 8. Engineering stress–strain curves for CP Ti (Grade-4) in different structural states.

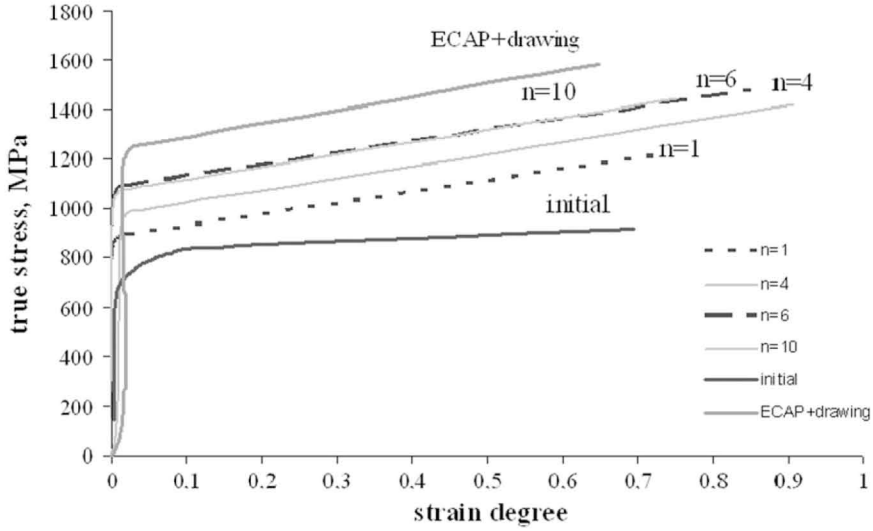

Fig. 9. True stress–true strain curves for CP-Ti in different structural states.

Acknowledgments

This work was carried out in the framework of the ViNaT project, Contract no. 295322, FP7-NMP-2011-EU-Russia, NMP.2011.1.4-5 coordinated with State Contract no. 16.523.12.3002 from the Russian Ministry of Education and Science on the Federal Target Program Research and Development under Priority Directions of Scientific-Technological Complex of Russia for 2007–2013. The work also has been partially supported by The Federal Target Program within the State Contract no. 11.519.11.3016. Experimental works were partly carried out at the Center for Collective Use of Scientific Equipment of Ufa State Aviation Technical University. IS would like to acknowledge the Spanish Ministry of Science and Innovation for the funding through the Ramon y Cajal Fellowship.

References

[1] D.M. Brunette, P. Tengvall, M. Textor, P. Thomsen, Titanium in Medicine, Springer, Berlin Heidelberg New York, 2001.
[2] R.Z. Valiev, R.K. Islamgaliev, I.V. Alexandrov, Prog. Mater. Sci. 45 (2000) 103–189.
[3] A.V. Sergueeva, V.V. Stolyarov, R.Z. Valiev, A.K. Mukherjee, Scr. Mater. 45 (2001) 747–752.
[4] R.Z. Valiev, A.V. Sergueeva, A.K. Mukherjee, Scr. Mater. 49 (2003) 669–674.
[5] V.V. Stolyarov, L.O. Shestakova, A.I. Zharikov, V.V. Latysh, R.Z. Valiev, Y.T..Zhu, T.C. Lowe, Proceedings of the 9th International Conference on Titanium-99, vol. 1, 2001, pp. 466–472.
[6] V.V. Stolyarov, Y.T. Zhu, I.V. Alexandrov, T.C. Lowe, R.Z. Valiev, Mater. Sci. Eng. A 299 (2001) 59–67.
[7] I. Sabirov, M.T. Perez-Prado, J.M. Molina-Aldareguia, I.P. Semenova, G.Kh. Salimgareeva, R.Z. Valiev, Scr. Mater. 64 (2011) 69–72.
[8] I.P. Semenova, E.B. Yakushina, V.V. Nurgaleeva, R.Z. Valiev, Int. J. Mater. Res. 100 (2009) 1691–1696.
[9] K. Topolski, H. Garbacz, K.J. Kurzydlowski, Mater. Sci. Forum 584–586 (2008) 777–782.
[10] S. Zherebtsov, W. Lojkowski, A. Mazur, G. Salishchev, Mater. Sci. Eng. A 527 (2010) 5596–5603.
[11] D.K. Yang, P.D. Hodgson, C.E. Wen, Scr. Mater. 63 (2010) 941–944.
[12] Y.G. Ko, D.H. Shin, K.T. Park, C.S. Lee, Scr. Mater. 54 (2006) 1785–1789.
[13] G.I. Raab, E.P. Soshnikova, R.Z. Valiev, Mater. Sci. Eng. A 387–389 (2004) 674–677.
[14] A.A. Popov, I.Yu. Pyshmintsev, S.L. Demakov, A.G. Illarionov, T.C. Lowe, R.Z. Valiev, Scr. Mater. 37 (1997) 1089–1094.

[15] R.K. Islamgaliev, V.U. Kazykhanov, L.O. Shestakova, A.V. Sharafutdinov, R.Z. Valiev, Mater. Sci. Eng. A 493 (2008) 190–194.
[16] W. Pachla, M. Kulczyk, M. Sus-Ryszkowska, A. Mazur, K.J. Kurzydlowski, J. Mater. Process. Technol. 205 (2008) 173–182.
[17] G.G. Yapici, I. Karaman, H.J. Maier, Mater. Sci. Eng. A 434 (2006) 294–302.
[18] J. Gubicza, Zs. Fogarassy, Gy. Krallics, J. Labar, T. Torkoly, Mater. Sci. Forum 589 (2008) 99–104.
[19] V.V. Stolyarov, L. Zeipper, B. Mingler, M. Zehetbauer, Mater. Sci. Eng. A 476 (2008) 98–105.
[20] G.I. Raab, R.Z. Valiev, T.C. Lowe, Y.T. Zhu, Mater. Sci. Eng. A 382 (2004) 30–34.
[21] Y.T. Zhu, T.C. Lowe, R.Z. Valiev, G.I. Raab, Continuous Equal-Channel Angular Pressing, US Patent no. 7,152,448, USC 72/262, Los Alamos National Security, LLC (Los Alamos, NM), filed December 16 2004, issued December 26 2006.
[22] A.V. Polyakov, D.V. Gunderov, G.I. Raab, Mater. Sci. Forum 667–669 (2011) 1165–1170.
[23] H.S. Kim, Mater. Sci. Eng. A 328 (2002) 317–323.
[24] I.J. Beyerlein, L.S. Tóth, Prog. Mater. Sci. 54 (2009) 427–510.
[25] P. Van Houtte, A.K. Kanjarla, A. Van Bael, M. Seefeldt, L. Delannay, Eur. J. Mech. A 25 (2006) 634–648.
[26] A.A. Smolyakov, V.P. Solovyev, A.I. Korshunov, N.A. Enikeev, Mater. Sci. Eng. A 493 (2008) 148–159.
[27] J. Segurado, R.A. Lebensohn, J. Llorca, C.N. Tome, Int. J. Plast. 28 (2012) 124–140.
[28] L.S. Tóth, Y. Estrin, R. Lapovok, C. Gu, Acta Mater. 58 (2010) 1782–1794.
[29] M. Seefeldt, L. Delannay, B. Peeters, E. Aernoudt, P. Van Houtte, Acta Mater. 49 (2001) 2129–2143.
[30] A.A. Nazarov, N.A. Enikeev, A.E. Romanov, T.S. Orlova, I.V. Alexandrov, I.J. Beyerlein, R.Z. Valiev, Acta Mater. 54 (2006) 985–995.
[31] Y. Estrin, L.S. Tóth, A. Molinari, Y. Bréchet, Acta Mater. 46 (1998) 5509–5522.
[32] I. Alexandrov, R. Chembarisova, V. Sitdikov, V. Kazyhanov, Mater. Sci. Eng. A 493 (2008) 170–175.
[33] H.S. Kim, Y. Estrin, Mater. Sci. Eng. A 410–411 (2005) 285–289.
[34] E. Schafler, M. Zehetbauer, T. Ungar, Mater. Sci. Eng. A 319–321 (2001) 220–223.
[35] "LaboTex"—The Texture Analysis Software for Windows, 〈http://www.labosoft.com.pl〉.
[36] J. Gubicza, T. Ungar, Z. Kristallogr. 222 (2007) 114–128.
[37] H.P. Lee, C. Esling, H.J. Bunge, Textures Microstruct. 7 (1988) 317–337.
[38] D.H. Shin, I. Kim, J. Kim, Y.S. Kim, S.L. Semiatin, Acta Mater. 51 (2003) 983–996.
[39] S. Nemat-Nasser, W.G. Guo, J.Y. Cheng, Acta Mater. 47 (1999) 3705.
[40] E.C. Oliver, M.R. Daymond, J. Quinta Da Fonseca, P.J. Withers, J. Neutron Res. 12 (2004) 33–37.
[41] I. Sabirov, R.Z. Valiev, I.P. Semenova, R. Pippan, Metall. Mater. Trans. A 41 (2010) 727–733.